

PAPER

View Article Online
View Journal | View IssueCite this: *J. Mater. Chem. A*, 2015, 3, 20527Iron(II) molybdate (FeMoO_4) nanorods as a high-performance anode for lithium ion batteries: structural and chemical evolution upon cycling†Zhenyu Zhang,^{‡a} Wenyue Li,^{‡b} Tsz-Wai Ng,^a Wenpei Kang,^a Chun-Sing Lee^a and Wenjun Zhang^{*a}

FeMoO_4 nanorods were synthesized by a one-step solvothermal method and demonstrated to have attractive performance as an anode material in lithium ion batteries (LIBs). The specific capacity of the electrode exhibited an initial fading in the first 50 cycles and subsequently recovered to 1265 mA h g^{-1} at about the 500th cycle at a rate of 1C, after that, the capacity remained stable around 1110 mA h g^{-1} until the 1000th cycle. Based on comprehensive analysis of the structural and chemical evolution at each stage of capacity variation, we illustrated that the FeMoO_4 nanorods were converted to a $\text{Fe}_2\text{O}_3/\text{MoO}_3$ mixture after the first cycle and they experienced gradual structural variation of grain refinement and amorphization with their morphology transformed from nanorods to nanosheets upon cycling. Such changes in the chemical composition and microstructure of nanorods led to larger effective surface area, improved electrochemical reaction kinetics, and capacity retention capability. As a similar tendency of the specific capacity upon cycling has been widely observed for metal oxide anodes, studies on structural and chemical evolution of electrode materials during the whole cyclic life will be helpful for understanding their electrochemical reaction mechanism and provide guidance to material design and structural optimization of electrodes.

Received 25th July 2015
Accepted 31st August 2015

DOI: 10.1039/c5ta05723j

www.rsc.org/MaterialsA

Introduction

To meet the requirements of high energy and power densities, and long life span of lithium ion batteries (LIBs), exploiting new anode materials with high theoretical capacity and optimal micro- or nano-scale structures has been an important research topic. Due to the higher reversible capacities over the commercially used graphite, ternary metal oxides (TMOs) have attracted extensive research interest as alternative anode materials for LIBs.^{1–3} Molybdenum-containing TMOs are an important family for anode application because of the high oxidation state of molybdenum.⁴ For instance, CuMoO_4 ,⁵ MnMoO_4 ,⁶ NiMoO_4 ,⁷ and CoMoO_4 (ref. 8) have been demonstrated to be promising electrode materials for LIBs. However, as an important member of metal molybdates, FeMoO_4 has only been studied for its electrochemical applications, such as in electrodes for oxygen evolution,⁹ supercapacitors,^{10,11}

hydrodesulfurization catalysis,¹² and cathode materials for LIBs.⁵ Although FeMoO_4 has a high theoretical capacity of $992.3 \text{ mA h g}^{-1}$ due to the high valences of Fe (+3) and Mo (+6), there have been few investigations on FeMoO_4 as an anode material for LIBs until now. Only very recently, Ju *et al.* reported that FeMoO_4 nanocubes could be used as an efficient and reversible lithium storage anode material which exhibits 926 mA h g^{-1} after 80 cycles at a current density of 100 mA g^{-1} ($\sim 0.1\text{C}$, $1\text{C} = 992.3 \text{ mA g}^{-1}$) and remarkable rate performance, indicating a good prospect of FeMoO_4 for LIB application.¹³

It has been widely accepted that the capacitance of anode materials upon cycling is largely determined by their chemical and structural stabilities during charge/discharge processes.^{14,15} For the anode materials in LIBs, such as C, Si, and Sn, it has been usually found that the specific capacity decreased monotonically with the cycling process due to the mechanical degradation and chemical composition variation by the repeated volume change. However, for TMO anode materials, an increase of the capacity was, in general, observed after an initial capacity fading, which was illustrated by the activation process of electrode materials.^{16–22} For instance, vesiculation was observed in $\gamma\text{-Fe}_2\text{O}_3/\text{C}/\text{MWNT}$ composites²³ which resulted in an increased active surface area; Co_3O_4 hollow spheres²⁴ were shown to transform to mesoporous amorphous nanospheres consisting of enlarged pore size/space and flower-like nanosheets during electrode activation, which delivered increased capacities along

^aCenter of Super-Diamond and Advanced Films (COSDAF), Department of Physics and Materials Science, City University of Hong Kong, Hong Kong, P. R. China. E-mail: apwjzh@cityu.edu.hk

^bFunctional Thin Films Research Centre, Shenzhen Institute of Advanced Technology, Chinese Academy of Sciences, Shenzhen 518055, P. R. China

† Electronic supplementary information (ESI) available. See DOI: 10.1039/c5ta05723j

‡ These authors contributed equally to this work.

with cycles. These results suggest that, in contrast to the conventional electrode materials, certain structure and chemical composition variations of TMO electrodes are beneficial to the improvement of electrochemical performance. Therefore, further investigation on the evolution of electrode materials during the whole life of batteries is required to understand the electrochemical reaction mechanism and improve the battery performances of TMOs.

In this work, we synthesized FeMoO₄ nanorods by a one-step solvothermal method, and demonstrated that they exhibited high capacity and long-term cycling stability as an anode material for LIBs. At a current density of 1C, the battery capacity experienced a fast drop to $\sim 400 \text{ mA h g}^{-1}$ in the first ~ 50 cycles, then it gradually increased up to $\sim 1200 \text{ mA h g}^{-1}$ at the $\sim 500^{\text{th}}$ cycle, and maintained at 1100 mA h g^{-1} until the 1000^{th} cycle. In order to understand the electrochemical characteristics during long-term cycling, the anode materials at several critical stages were carefully analyzed by employing transmission electron microscopy (TEM), Raman spectroscopy, X-ray photoelectron spectroscopy (XPS) and electrochemical analysis. Based on that, the relationship of the structural/chemical composition evolution of FeMoO₄ nanorod anodes during cycling with the electrode performance was demonstrated.

Experimental section

Synthesis

The FeMoO₄ nanorods were synthesized by a one-step solvothermal method. Typically, a solution of 0.08 M FeCl₂·4H₂O in triethylene glycol (TEG) was added dropwise into an aqueous solution of 0.08 M Na₂MoO₄·2H₂O during magnetic stirring. The red brown mixed solution was then transferred into a Teflon-lined stainless steel autoclave and maintained at 120 °C for 24 h in an electrical oven. After naturally cooling to room temperature, the precipitate was collected by centrifugation, washed several times with deionized water and ethanol, and vacuum dried at 60 °C for 12 h.

Characterization

The product was first characterized by using SEM (Philips XL30 FEG), TEM (Philips FEG CM200, operating at 200 kV), and powder XRD (Philips X'Pert) using CuK α radiation ($\lambda = 0.15418 \text{ nm}$) with a scanning step of $0.05^\circ \text{ s}^{-1}$. XPS analysis was performed using a VG ESCALAB 220i-XL UHV surface analysis system with a monochromatic Al K α X-ray source (1486.6 eV). Raman spectra were measured using a Renishaw 2000 Raman microscope with a laser wavelength of 633 nm. The nitrogen adsorption-desorption isotherms of the FeMoO₄ nanorods were conducted on a Quantachrome NovaWin Nova Station A, from which the specific surface area and pore size distribution curves of the samples were obtained by the Barrett-Joyner-Halenda (BJH) method.

Electrochemical tests

The anodes for LIBs were made by mixing active materials (FeMoO₄ nanorods), a conductivity agent (carbon black) and a

binder (polyvinylidene fluoride) in a weight ratio of 80 : 10 : 10, and coating the mixture on a copper foil with a total weight loading of $1.2 \pm 0.3 \text{ mg cm}^{-2}$ which was then vacuum-dried at 60 °C for 12 h. Coin cells (CR2032) were fabricated with lithium metal as the counter electrode, Celgard 2400 as the separator, and LiPF₆ (1 M) in ethylene carbonate/dimethyl carbonate (EC/DMC, 1 : 1 vol%) as the electrolyte, which were assembled in an Ar-filled glovebox (MBRAUN) followed by 24 h aging treatment before the test. CV measurements were carried out at a scan rate of 0.1 mV s^{-1} within the range of 0.01–3.0 V with an electrochemical workstation (CHI 600D). EIS was performed by using a ZAHNER-elektrik IM 6 electrochemical system over a frequency range from 100 KHz to 10 mHz. The charge-discharge measurements of cells were carried out within a fixed voltage window of 0.01–3.0 V by using a battery test system (MACCOR 4000) at room temperature. At different points during the battery test, the cells were stopped and disassembled and the working electrodes were washed using deionized water, ethanol and acetone, separately. The corresponding cycling curves of the stopped batteries are shown in Fig. S1.† After being dried in a vacuum oven, the anode materials were collected for TEM, Raman spectroscopy and XPS observations.

Results and discussion

Composition and structure characterization

Fig. 1(a) shows the scanning electron microscopy (SEM) image of FeMoO₄ nanorods synthesized by a one-step solvothermal method. The nanorods have a length in the range of 300–500 nm and a diameter of 50–100 nm. The energy dispersive spectroscopy (EDS) measurements in Fig. S2† reveal that the nanorods are composed of Fe, Mo, and O in a ratio of about 1 : 1 : 6. Fig. 1(b) depicts a typical X-ray diffraction (XRD) pattern of the as-prepared nanorods, which matches well with the standard diffractions of monoclinic β -FeMoO₄ (JCPDS # 22-0628); and two weaker diffraction peaks at 28.2° and 40.9° (denoted with stars) are also detected, which can be assigned to -220 and -223 planes of α -FeMoO₄ (JCPDS # 22-1115). The XRD measurements indicate that the sample mainly comprises a β -FeMoO₄ phase with a small amount of α -FeMoO₄ impurity. TEM observations in Fig. 1(c) and its inset verify that the FeMoO₄ nanorods are mesoporous with a pore size of $\sim 10 \text{ nm}$ in diameter. The nitrogen adsorption-desorption test further revealed a specific surface area of $84.2 \text{ m}^2 \text{ g}^{-1}$, and a pore size distribution around 10 nm by using the BJH method (Fig. S3†), which is consistent with the TEM observations. Fig. 1(d) shows the high-resolution TEM (HRTEM) image obtained on the same nanorod. The marked lattice fringes with d -spacing of 0.34 and 0.33 nm agree well with the -220 and -202 planes of the β -FeMoO₄ crystal. The corresponding electron diffraction pattern taken along the zone axis of $[111]$ suggests the single crystal nature of the nanorod.

By stopping the solvothermal reaction after different durations, we studied the growth process of the FeMoO₄ nanorods. As suggested by the XRD patterns (Fig. S4†), during the whole growth procedure, both α and β phases of FeMoO₄ exist in the samples. However, the content of the β phase increased

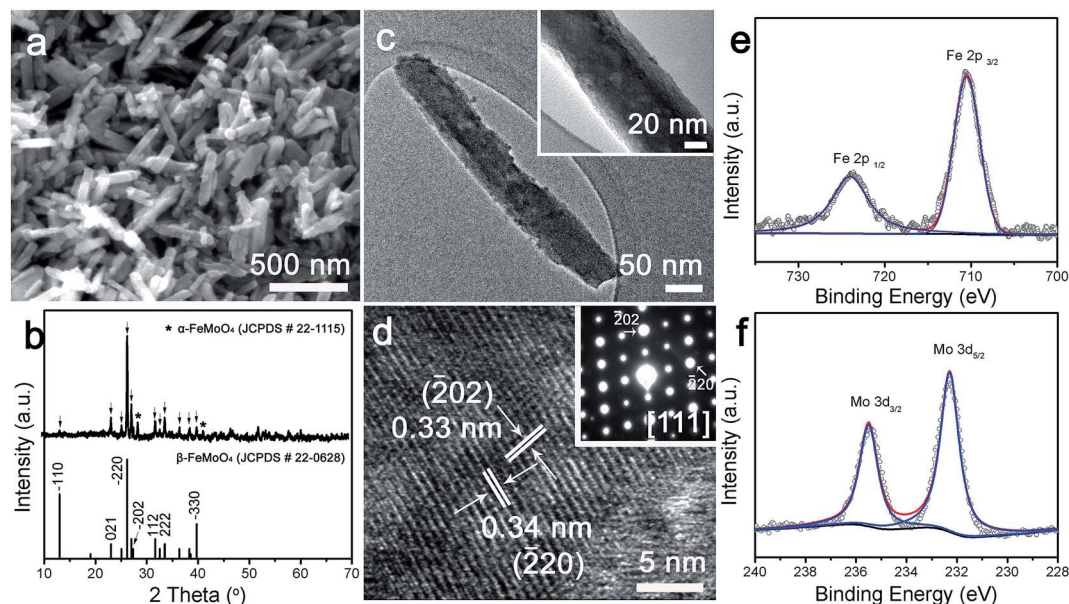


Fig. 1 (a) SEM image and of the FeMoO_4 nanorods. (b) XRD pattern of the sample with reference to the standard diffractions of $\beta\text{-FeMoO}_4$. (c) TEM image of an individual FeMoO_4 nanorod and the inset is the enlarged image. (d) HRTEM image of a nanorod with marked lattice fringes. The inset is the electron diffraction pattern of the nanorod. The high-resolution XPS (e) Fe 2p spectrum and (f) Mo 3d spectrum of the sample.

gradually with the reaction time, and the majority of the sample after reaction for 24 hours is in the β phase.¹³ In the SEM and TEM observations (Fig. S5[†]), it was revealed that FeMoO_4 nanoparticles of 50–100 nm in size were formed after 1 h, and the nanoparticles were developed to nanorods as the reaction time was extended to 4 h. At this stage, the nanorods had a rough surface with some nanoparticles attached. These nanoparticles were suggested to be the precursors for the formation of FeMoO_4 nanorods,²⁵ and they aggregated at the end of nanorods growing along the [121] direction. Nanorods with a smooth surface and porous interior were observed as the reaction was prolonged to 12 hours, further extending the reaction time did not show a significant change in the dimension, morphology, and porous structure of nanorods.

XPS was also carried out to study the chemical composition of nanorods. The survey spectrum in Fig. S6[†] confirms that the sample contains Fe, Mo, and O, and the atomic ratio of Fe/Mo is about 1 : 1. The high-resolution Fe 2p and Mo 3d XPS spectra are presented in Fig. 1(e) and (f), respectively. The peaks at 710.5 and 724.1 eV for $\text{Fe } 2p_{3/2}$ and $\text{Fe } 2p_{1/2}$ indicate the Fe^{2+} oxidation state; and Mo 3d peaks at binding energies of 232.3 and 235.5 eV suggest the Mo^{6+} oxidation state.²⁵ The deconvolution of the O 1s peaks, as shown in Fig. S7,[†] reveals two components at 530.4 and 531.9 eV, which are assigned to the lattice oxygen and chemisorbed oxygen, respectively. The XPS results confirm the formation of FeMoO_4 , which is consistent with the EDS and XRD results.¹¹

Electrochemical performances

The cycling performance of FeMoO_4 nanorods as the anode for a LIB was tested by galvanostatic charge–discharge measurements at a rate of 1C. As shown in Fig. 2(a), despite a high initial

discharge capacity, the capacity faded tremendously from 1134 (2^{nd} cycle) to 451 mA h g^{-1} (50^{th} cycle). The drastic capacity decrease in this period was ascribed to the continuous and irreversible consumption of electrode materials for the formation of a solid electrolyte interface (SEI) layer.²⁴ Then the capacity started to increase gradually until an utmost value of 1265 mA h g^{-1} was reached at about the 500^{th} cycle. Noticeably, the capacity is over 300% larger than the theoretical capacity of a traditional graphite anode ($\sim 370 \text{ mA h g}^{-1}$), and it is also higher than the theoretical capacity of FeMoO_4 ($992.3 \text{ mA h g}^{-1}$). After that, the capacity reduced again at a relatively low rate but still maintained higher than 1110 mA h g^{-1} until the 1000^{th} cycle. Correspondingly, the coulombic efficiency increased from 70% in the first cycle to above 99% after the 50^{th} cycle, which could be considered as an indication of the formation of a stable SEI layer after 50 cycles.²⁶

As suggested by the long-term cycling performance, the critical capacitance points at 50^{th} , 500^{th} , and 1000^{th} cycles in the battery life were selected for further investigation. We tested the rate capabilities of the FeMoO_4 nanorod anode by using stepped rates of 1C, 2C, 5C, 10C, 1C, and 0.1C at different stages around 50^{th} , 500^{th} , and 1000^{th} cycles (termed as stages I, II, and III, respectively), as depicted in Fig. 2(b) and (c). The 1C capacitance exhibited a similar trend to that shown in Fig. 2(a), and the rate performance of the electrode showed the same characteristics at these stages, *i.e.*, the capacities decreased as the current density increased from 1C to 10C, and they recovered to almost their original values as the current density was switched back to 1C. Further decreasing the current density to 0.1C led to even higher capacities. However, close observation of the enlarged views in Fig. 2(c) revealed slight differences between the rate performances at different stages. When the current density

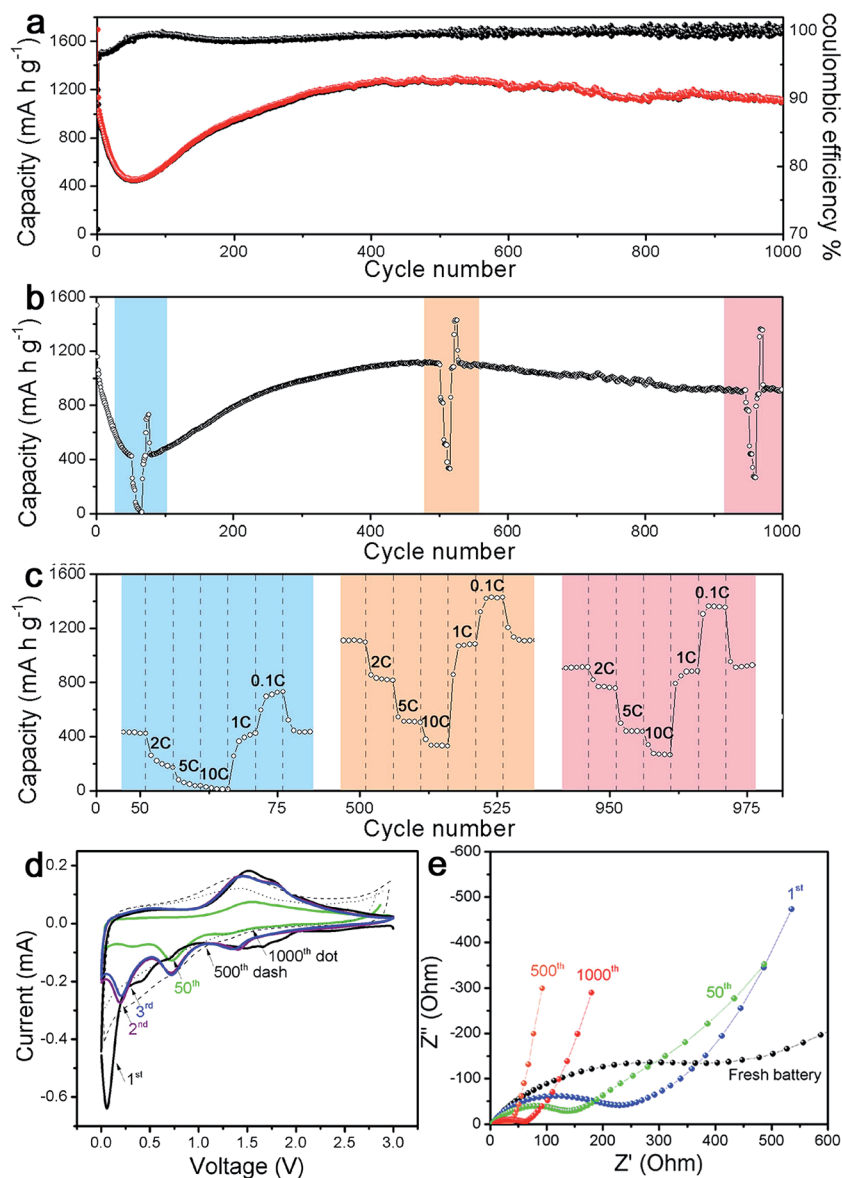


Fig. 2 (a) Cycling performance and coulombic efficiency of the FeMoO₄ nanorod anode at a rate of 1C in 1000 cycles. (b) Rate capability test of the FeMoO₄ nanorod anode at the rates of 1C, 2C, 5C, 1C, 10C, and 0.1C and at different stages (stage I, II, and III correspond to that around the 50th, 500th, and 1000th cycle, respectively) of cycling. (c) Enlarged plot areas of the cycle stages I, II and III for clearer observation. (d) CV curves obtained on the cells for the first three cycles, and after 50, 500, and 1000 cycles at galvanostatic charge-discharge. (e) EIS spectra of the freshly fabricated cell, and the cells subjected to 1, 50, 500, and 1000 galvanostatic charge-discharge cycles with a rate of 1C.

decreased from 10C to 1C or from 0.1C to 1C, the capacities in stage II and III could recover more rapidly to their initial capacity values as compared with those in stage I. It is known that the rate capability depends strongly on both electron and ion conductivities of the electrode,²⁷ the improved rate capability in stage II and III should be due to the structural evolution of FeMoO₄ nanorods as discussed below.

Cyclic voltammetry (CV) and electrochemical impedance spectroscopy (EIS) measurements of the batteries at the corresponding stages were also performed. Fig. 2(d) displays the CV curves obtained for the 1st, 2nd, 3rd, 50th, 500th, and 1000th cycles of the galvanostatic charge-discharge process. For the cathodic curves, several peaks were observed: (i) the peak around 0.1 V in

the first discharge was attributed to the irreversible formation of the SEI layer,⁸ and it gradually disappeared after 50 cycles; (ii) the broad peak between 1.5 and 2.0 in the first discharge was assigned to the irreversible intercalation of lithium ions into the crystal lattice, which also disappeared in the following cycles;²⁸ (iii) starting with the 2nd cycle, the peak around 0.7 V was due to the reduction of Fe²⁺ or Fe³⁺ to Fe⁰,^{16,19} which maintains its intensity until the 50th cycle, and it could still be distinguished after 500 cycles; (iv) the peaks in the ranges of 0.2–0.4 V and 1.2–1.4 V were associated with the multi-step reduction of Mo⁶⁺ to Mo⁰, which are also evident in the 50th and 500th cycles.^{28,29} Correspondingly, in the anodic curves, two broad peaks around 1.5 and 1.8 V ascribed to the oxidation of Fe and Mo metals were

observed in the first cycle, and they merged to a broad peak around 1.5 V after 50 cycles. In the 500th and 1000th cycles, the peak gradually shifted to a lower potential of ~ 1.4 V, implying the alleviating polarization after the 50th cycle.³⁰ Since the integrated peak area was equal to the capacity,³¹ the current intensity of the CV curve at the 500th cycle is the highest, agreeing with the cycling performance shown in Fig. 2(a).

Fig. 2(e) presents the EIS interceptions of the freshly fabricated cell, and the cells after testing for 1, 50, 500, and 1000 galvanostatic charge–discharge cycles at a rate of 1C. All the Nyquist plots exhibited a semicircle in the high frequency region followed by a straight line in the low frequency region, being related to the interface charge transfer process and diffusion process, respectively. It is apparent that the charge transfer resistance (R_{ct}) persistently decreased until the 500th cycle, *i.e.*, from $\sim 438\ \Omega$ for a freshly fabricated cell to $\sim 23\ \Omega$ at the 500th cycle, and then increased slightly to $\sim 54\ \Omega$ at the 1000th cycle (the fitting results and equivalent circuits are shown in Table S1†). The decreasing R_{ct} in the 500 cycles indicates the activation of electrodes and improved kinetics of the reaction.³² In addition, the fitted surface film resistance (R_f) and Warburg impedance (Z_w) show a generally decreasing trend during cycling, except for the abnormal increase in the 50th cycle. This suggests that the diffusion resistance of lithium ions increased around the 50th cycle due to the formation of thick and unstable SEI layers over the nanorods.^{33,34} After that, as discussed below, the polycrystalline nanorods gradually changed to an amorphous state with refined grains and finally converted to nanosheets, and thinner and stable SEI layers were grown on the nanosheet surfaces, which was beneficial for the lithium insertion/extraction and electron transfer processes.^{24,34} The EIS measurements are in accordance with the alleviated

polarization effect at the 50th cycle (from CV curves) and improved rate performance after the 50th cycle.

Structural and chemical evolution

The morphological transformation of the electrode materials was systematically investigated at each critical stage of the charge/discharge process. Fig. 3 shows a set of TEM images showing the morphology evolution of FeMoO₄ nanorods at different stages of the cycling (1st, 50th, 500th, and 1000th cycles) at a rate of 1C. After one cycle, the FeMoO₄ nanorods had no obvious change (Fig. 3(a)). However, the enlarged view in the inset in Fig. 3(a) revealed increased porosity of nanorods. The HRTEM image and the corresponding fast Fourier transform (FFT) pattern in Fig. 3(b) further showed reduced crystallinity after the first lithium ion intercalation. After 50 cycles, the nanorods presented a rough surface composed of a large amount of nanoparticles and an enlarged pore size/space, as shown in Fig. 3(c). The transformation of nanorods to a polycrystalline structure is apparently evidenced in the HRTEM image and the corresponding FFT pattern in Fig. 3(d). The fragmentation of the nanorod surface and continuous formation of the SEI layer are responsible for the drastic specific capacitance fading during the period of the first 50 cycles. Moreover, the SEI layer at this stage is thick and unstable (also suggested by ref. 23), resulting in an increased ion diffusion resistance, serious polarization and bad rate performance. Fortunately, after the initial 50 cycles, a stable SEI layer was formed as indicated by the stabilized coulombic efficiency, which led to the recovery of electrochemical performance of the battery.

From the 50th to ~ 500 th cycle, the nanorods were gradually transformed to nanosheets with further grain refinement,

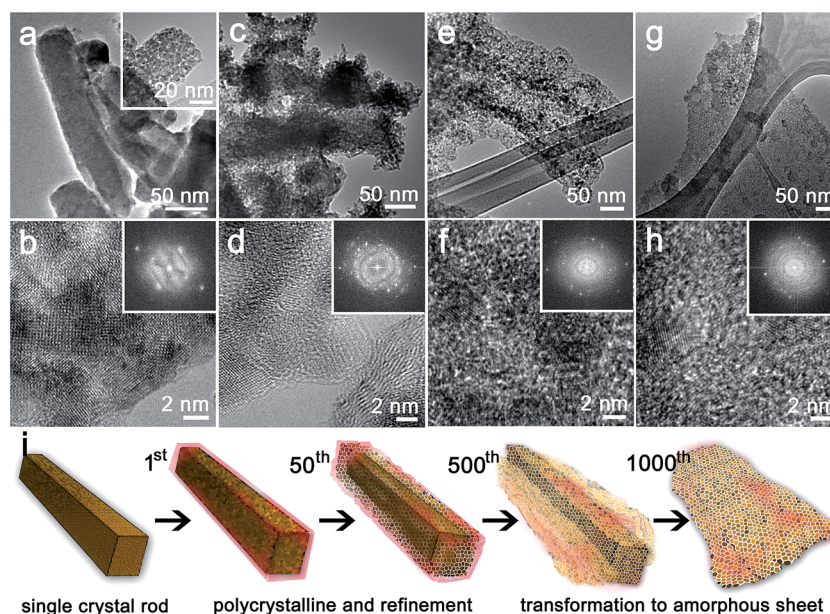


Fig. 3 TEM and corresponding HRTEM images of the FeMoO₄ nanorod electrode material after various battery cycles (a and b) 1, (c and d) 50, (e and f) 500, and (g and h) 1000, insets are their FFT patterns. (i) Schematic diagram of the morphology evolution of FeMoO₄ nanorods with cycles.

bringing about large quantities of pores and a larger surface area as shown in Fig. 3(e). High-density backbones could still be distinguished in the center of nanosheets which comprised amorphous materials and small crystals, as observed in Fig. 3(f) and the corresponding FFT pattern in the inset. The formation of nanosheets could be more clearly observed in the SEM images in Fig. S8.† Accordingly, such a structural transformation results in a gradual capacity increase in the following 500 cycles, together with the enhanced rate performance, alleviated polarization, and largely reduced charge transfer and diffusion resistances. Impressively, for the 1000th cycle, nanorods have been completely converted to nanosheets with an average size of several hundreds of nanometers (Fig. 3(g) and Fig. S8†). As indicated by the FFT pattern and HRTEM image (Fig. 3(h)), the layer is in an amorphous state with nanocrystals of ~5 nm in size embedded. These porous and amorphous layers with a larger specific surface area as compared with the original nanorods are believed to provide increased Li⁺ active sites and enable improved reaction kinetics. Furthermore, the distributions of O, Fe and Mo elements were studied by using high-angle annular dark-field scanning transmission electron microscopy (HAADF-STEM) and EDS elemental mapping at 1st, 50th, 500th and 1000th cycles (Fig. S9†). It was demonstrated that these elements were distributed uniformly over the nanorods at different stages. As a result, the capacity maintained stable against the repeated charge–discharge cycling and had enhanced rate capability. As illustrated by the schematic diagram in Fig. 3(i), the original FeMoO₄ nanorods experienced structural transformation from single crystals to a polycrystalline state with refined grains, and finally converted to amorphous nanosheets. The morphology evolution was driven by the electrochemical reactions and the continuous expansion and contraction of the metal oxide species in the discharge and charge process, which are closely related to the electrochemical performance of the electrode at different stages.

For the purpose of identifying the chemical reactions during the charge and discharge process, the electrode materials after different cycles were investigated by Raman spectroscopy and XPS. Fig. 4(a) displays the Raman spectra of the as-prepared FeMoO₄ nanorods and those after charge/discharge for 1, 50, 500, and 1000 cycles. For the pristine nanorods, the peaks at 823, 879 and 926 cm⁻¹ (as marked by diamonds) are assigned to FeMoO₄.¹⁰ In the subsequent cycles, a few new peaks are observed. For instance, peaks at 225, 293 and 416 cm⁻¹ are assigned to Fe₂O₃ (as marked by club);³⁵ the broad peak at 1330 cm⁻¹ may come from conductive agent carbon (~1350 cm⁻¹ as marked by spade) in the electrode and two-magnon scattering of Fe₂O₃ (~1320 cm⁻¹); and the peaks at 369, 660, 811 and 987 cm⁻¹ are attributed to MoO₃ (marked with heart).³⁶ These peaks with considerable relative intensities could still be revealed until the 50th cycle, implying the existence of Fe₂O₃ and MoO₃ phases during the first 50 cycles. However, the peaks disappeared in the spectra for the 500th and 1000th cycles, leaving only the carbon signal at 1350 cm⁻¹. XRD measurements of the samples were also performed after the charge and discharge processes, as depicted in Fig. S10.† The results agree with those drawn from the Raman and TEM characterization very well: (1)

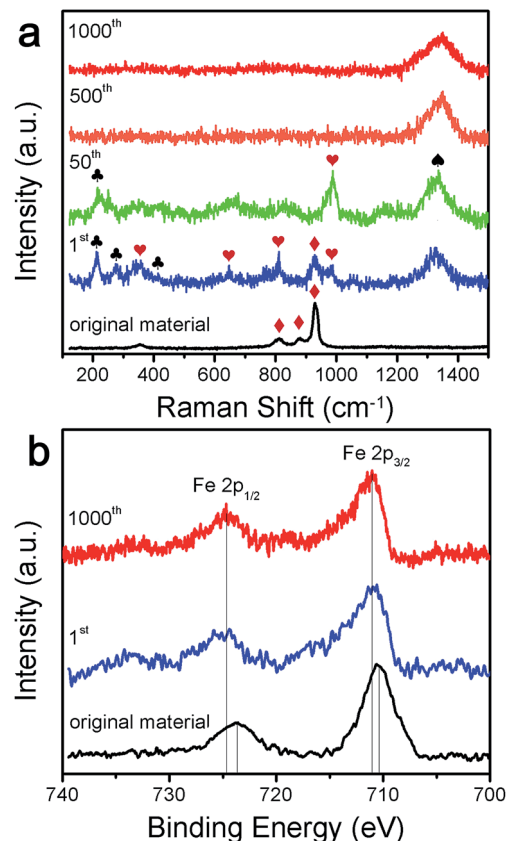
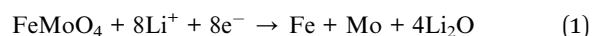


Fig. 4 (a) Raman spectra of the original FeMoO₄ nanorods and the electrode material after different cycles (1, 50, 500 and 1000). (b) The high-resolution Fe 2p XPS spectrum of the original FeMoO₄ nanorods, after the 1st cycle and the 1000th cycle.

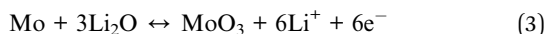
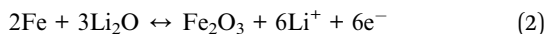
the original FeMoO₄ transformed to Fe₂O₃ and MoO₃ after the first cycle, and (2) the crystallinity of the electrode materials degraded along with the cycles and finally turned amorphous.

Fig. 4(b) depicts high-resolution Fe 2p XPS spectra collected from the pristine FeMoO₄ nanorods and electrode materials after 1 cycle and 1000 cycles. After the 1st cycle, both Fe 2p_{3/2} (710.5 eV) and Fe 2p_{1/2} (724.1 eV) were shifted to higher binding energies, *i.e.*, Fe 2p_{3/2} (711.1 eV) and Fe 2p_{1/2} (724.8 eV), respectively, implying that Fe²⁺ changed to the Fe³⁺ oxidation state after the first discharge–charge cycle.^{37,38} In contrast, the valence of the Mo element remains the same during the 1000 discharge–charge cycles, as suggested by the high-resolution Mo 3d XPS spectrum in Fig. S11.†

In the first discharge, the crystal structure of FeMoO₄ was destructed followed by the formation of metal nanoparticles in the amorphous matrix of Li₂O, as described by eqn (1).



According to the Raman spectroscopy and XPS results, this process is irreversible since binary metal oxides are detected in the following cycles. In the subsequent cycles, transformation between Fe and Mo metal particles and their respective metal oxides occurs reversibly, as shown in eqn (2) and (3).



The theoretical capacity of FeMoO_4 including the reduction of Mo^{6+} to Mo^0 and Fe^{2+} to Fe^0 by the lithium ions is calculated to be $992.25 \text{ mA h g}^{-1}$. After the reactivation process, the stabilized capacity reached up to 1265 mA h g^{-1} at about the 500th cycle, which is 25% higher than the theoretical capacity of FeMoO_4 . The oxidation of Fe^{2+} to Fe^{3+} should account for the even higher specific capacity as compared with the theoretical one. As a reference, the theoretical capacity of Fe_2O_3 (1117 mA h g^{-1}) is higher than that of FeO (744 mA h g^{-1}).^{34,39}

For the electrodes based on C, Si, and Sn, grain refinement (pulverization) and amorphization lead to the degradation of the electrode with reduced capacity and poor cycling stability. However, for the MO electrodes including TMOs, the grain refinement and amorphization may play positive roles in affecting the electrochemical performance of electrodes. (1) Previous research has suggested that amorphization of MO crystals leads to narrowed potential hysteresis and faster conversion reaction rates, and thus a more reversible electrochemical reaction than that of the crystalline phase could be achieved.^{31,40} Similarly, the transformation to the amorphous structure containing nanocrystals in our case should be beneficial for preventing the agglomeration of metal grains and improving the electrochemical reaction kinetics, resulting in much better cycling and rate performance than that with the initial crystal FeMoO_4 nanorods. (2) The increased lateral size of nanostructures, enhanced open-boundaries and effective interfacial area are significant for maintaining the high capacities.⁴¹ The increased lateral size of nanostructures, enhanced open-boundaries and effective interfacial area are vital for maintaining the high capacities. Due to the structural transformation of nanorods to amorphous layers, it is proposed that lithium ions and electrons are separately stored in the interfacial regions where lithium ions are collected at the phase boundaries, according to the suggested interfacial charging mechanism.^{42–44} Extra lithium ions could be accommodated in the interfacial space between the amorphous layers, leading to an improved reversible capacity, which became predominant along with cycling.

Conclusion

FeMoO_4 nanorods have been demonstrated as a high-performance anode material for LIBs, which exhibit superior cycling and rate performance as compared with conventional graphitic electrodes. Through elaborate investigation on the structural and chemical evolution process of the electrode materials by comprehensive characterization, a self-induced structural optimization (e.g., grain refinement with increased porosity and structure transformation from crystalline nanorods to amorphous nanosheets) has been exposed. Significantly, combining the development of electrochemical performance as cycles and structural and chemical evolution, we conclude that the structural transformation and amorphization of TMO electrode

materials improve the electrochemical reaction kinetics and increase valid surface areas, contributing to capacity fading, recovery and stabilization, which differs from the cases of electrodes based on elemental materials such as C, Si and Sn. The combined investigation between the observations and electrochemical analysis in this work may give a deeper understanding about the electrochemical reaction mechanism of the TMOs for the LIB anodes.

Acknowledgements

This work was financially supported by the National Natural Science Foundation of China (Grant No. 61176007 and 51372213).

References

- 1 G. G. Guo, H. B. Wu and X. W. Lou, *Adv. Energy Mater.*, 2014, **4**, 1400422.
- 2 L. Hu, H. Zhong, X. R. Zheng, Y. M. Huang, P. Zhang and Q. W. Chen, *Sci. Rep.*, 2012, **2**, 986.
- 3 W. P. Kang, Y. B. Tang, W. Y. Li, X. Yang, H. T. Xue, Q. D. Yang and C. S. Lee, *Nanoscale*, 2015, **7**, 225–231.
- 4 F. Wang, R. Robert, N. A. Chernova, N. Pereira, F. Omenya, F. Badway, X. Hua, M. Ruotolo, R. G. Zhang, L. J. Wu, V. Volkov, D. Su, B. Key, M. S. Whittingham, C. P. Grey, G. G. Amatucci, Y. M. Zhu and J. Graetz, *J. Am. Chem. Soc.*, 2011, **133**, 18828–18836.
- 5 N. N. Leyzerovich, K. G. Bramnik, T. Buhrmester, H. Ehrenberg and H. Fuess, *J. Power Sources*, 2004, **127**, 76–84.
- 6 S. S. Kim, S. Ogura, H. Ikuta, Y. Uchimoto and M. Wakihara, *Solid State Ionics*, 2002, **146**, 249–256.
- 7 W. Xiao, J. S. Chen, C. M. Li, R. Xu and X. W. Lou, *Chem. Mater.*, 2010, **22**, 746–754.
- 8 C. T. Cherian, M. V. Reddy, S. C. Haur and B. V. R. Chowdari, *ACS Appl. Mater. Interfaces*, 2013, **5**, 918–923.
- 9 R. N. Singh, J. P. Singh and A. Singh, *Int. J. Hydrogen Energy*, 2008, **33**, 4260–4264.
- 10 Y. H. Wang, P. He, W. Lei, F. Q. Dong and T. H. Zhang, *Compos. Sci. Technol.*, 2014, **103**, 16–21.
- 11 B. Senthilkumar and R. K. Selvan, *J. Colloid Interface Sci.*, 2014, **426**, 280–286.
- 12 J. L. Brito and A. L. Barbosa, *J. Catal.*, 1997, **171**, 467–475.
- 13 Z. C. Ju, E. Zhang, Y. L. Zhao, Z. Xing, Q. C. Zhuang, Y. H. Qiang and Y. T. Qian, *Small*, 2015, DOI: 10.1002/smll.201501294.
- 14 F. Lin, D. Nordlund, T. C. Weng, Y. Zhu, C. M. Ban, R. M. Richards and H. L. Xin, *Nat. Commun.*, 2014, **5**, 3358.
- 15 Y. G. Zhu, Y. Wang, Y. M. Shi, Z. X. Huang, L. Fu and H. Y. Yang, *Adv. Energy Mater.*, 2014, **4**, 1301788.
- 16 X. Gu, L. Chen, Z. C. Ju, H. Y. Xu, J. Yang and Y. T. Qian, *Adv. Funct. Mater.*, 2013, **23**, 4049–4056.
- 17 D. N. Wang, J. L. Yang, X. F. Li, D. S. Geng, R. Y. Li, M. Cai, T. K. Sham and X. L. Sun, *Energy Environ. Sci.*, 2013, **6**, 2900–2906.

- 18 J. S. Luo, J. L. Liu, Z. Y. Zeng, C. F. Ng, L. J. Ma, H. Zhang, J. Y. Lin, Z. X. Shen and H. J. Fan, *Nano Lett.*, 2013, **13**, 6136–6143.
- 19 X. Y. Li, Y. Y. Ma, L. Qin, Z. Y. Zhang, Z. Zhang, Y. Z. Zheng and Y. Q. Qu, *J. Mater. Chem. A*, 2015, **3**, 2158–2165.
- 20 Y. M. Sun, X. L. Hu, W. Luo and Y. H. Huang, *ACS Nano*, 2011, **5**, 7100–7107.
- 21 W. Wei, S. B. Yang, H. X. Zhou, I. Lieberwirth, X. L. Feng and K. Müllen, *Adv. Mater.*, 2013, **25**, 2909–2914.
- 22 Z. Y. Cai, L. Xu, M. Y. Yan, C. H. Han, L. He, K. M. Hercule, C. J. Niu, Z. F. Yuan, W. W. Xu, L. B. Qu, K. N. Zhao and L. Q. Mai, *Nano Lett.*, 2015, **15**, 738–744.
- 23 Y. F. Liu, J. M. Xu, X. Y. Qin, H. X. Xin, X. Q. Yuan, J. Zhang, D. Li and C. J. Song, *J. Mater. Chem. A*, 2015, **3**, 9682–9688.
- 24 H. T. Sun, G. Q. Xin, T. Hu, M. P. Yu, D. L. Shao, X. Sun and J. Lian, *Nat. Commun.*, 2014, **5**, 4526.
- 25 Z. Y. Zhang, C. G. Hua, M. Hashima, P. Chenb, Y. Q. Xiong and C. L. Zhang, *Mater. Sci. Eng., B*, 2011, **176**, 756–761.
- 26 W. M. Zhang, X. L. Wu, J. S. Hu, Y. G. Guo and L. J. Wan, *Adv. Funct. Mater.*, 2008, **18**, 3941–3946.
- 27 M. M. Kalantarian, S. Asgari and P. Mustarelli, *J. Mater. Chem. A*, 2014, **2**, 107–115.
- 28 P. J. Lu, M. Lei and J. Liu, *CrystEngComm*, 2014, **16**, 6745–6755.
- 29 X. Li, J. T. Xu, L. Mei, Z. J. Zhang, C. Y. Cui, H. K. Liu, J. M. Ma and S. X. Dou, *J. Mater. Chem. A*, 2015, **3**, 3257–3260.
- 30 T. Subburaj, K. Prasanna, K. J. Kim, P. R. Ilango, Y. N. Jo and C. W. Lee, *J. Power Sources*, 2015, **280**, 23–29.
- 31 J. C. Guo, Q. Liu, C. S. Wang and M. R. Zachariah, *Adv. Funct. Mater.*, 2012, **22**, 803–811.
- 32 Y. R. Zhong, M. Yang, X. L. Zhou, Y. T. Luo, J. P. Wei and Z. Zhou, *Adv. Mater.*, 2015, **27**, 806–812.
- 33 G. M. Zhou, D. W. Wang, L. C. Yin, N. Li, F. Li and H. M. Cheng, *ACS Nano*, 2012, **6**, 3214–3223.
- 34 Y. Ma, C. Zhang, G. Ji and J. Y. Lee, *J. Mater. Chem.*, 2012, **22**, 7845–7850.
- 35 M. V. Reddy, T. Yu, C. H. Sow, Z. X. Shen, C. T. Lim, G. V. S. Rao and B. V. R. Chowdari, *Adv. Funct. Mater.*, 2007, **17**, 2792–2799.
- 36 B. C. Windom, W. G. Sawyer and D. W. Hahn, *Tribol. Lett.*, 2011, **42**, 301–319.
- 37 T. Yamashita and P. Hayes, *Appl. Surf. Sci.*, 2008, **254**, 2441–2449.
- 38 Z. Y. Zhang, W. Y. Li, R. J. Zou, W. P. Kang, Y. S. Chui, M. F. Yuen, C. S. Lee and W. J. Zhang, *J. Mater. Chem. A*, 2015, **3**, 6990–6997.
- 39 Y. M. Sun, X. L. Hu, W. Luo, F. F. Xia and Y. H. Huang, *Adv. Funct. Mater.*, 2013, **23**, 2436–2444.
- 40 O. Delmer, P. Balaya, L. Kienle and J. Maier, *Adv. Mater.*, 2008, **20**, 501–505.
- 41 S. B. Yang, Y. Sun, L. Chen, Y. Hernandez, X. L. Feng and K. Müllen, *Sci. Rep.*, 2012, **2**, 427.
- 42 Q. Wang, J. Sun, Q. Wang, D. A. Zhang, L. L. Xing and X. Y. Xue, *J. Mater. Chem. A*, 2015, **3**, 5083–5091.
- 43 W. Wang, D. A. Zhang, W. Wang, J. Sun, L. L. Xing and X. Y. Xue, *Electrochim. Acta*, 2014, **146**, 411–418.
- 44 J. Maier, *Faraday Discuss.*, 2007, **134**, 51–66.